Fuel Processing Technology 253 (2024) 108027

Contents lists available at ScienceDirect

Fuel Processing Technology

journal homepage: www.elsevier.com/locate/fuproc

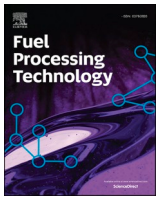

Tailoring the temperature coefficient of resistance of flame-formed carbon nanoparticle thin films by electric field-assisted deposition

A. Parisi [a,1], P. Darvehi [b,1], G. De Falco [a,*], M. Sirignano [a], M. Commodo [b,*], F. Di Natale [a], P. Minutolo [b]

[a] Dipartimento di Ingegneria Chimica, dei Materiali e della Produzione Industriale - Università degli Studi di Napoli Federico II, P.le Tecchio 80, 80125 Napoli, Italy
[b] Istituto di Scienze e Tecnologie per l'Energia e la Mobilità Sostenibili, Consiglio Nazionale delle Ricerche, P.le Tecchio 80, 80125 Napoli, Italy

ARTICLE INFO

Keywords:
Flame synthesis
Carbon nanoparticles
Nanostructured thin film
Optical and electrical characterization
Electric field deposition
Temperature coefficient of resistance

ABSTRACT

The electric-field assisted deposition is successfully proposed as a method for the manufacturing of carbon nanostructured films with tunable properties, benefiting from the superimposition of electric fields on the thermophoretic deposition. Morphology, optical, and thermo-resistive properties of the carbon nanoparticle (CNP) films have been studied by UV–vis Absorption Spectroscopy, Scanning Electron Microscopy, Atomic Force Microscopy, and Current-Voltage analysis. In comparison to thermophoresis alone, the introduction of an electric field results in a six-fold increase in the deposition rate characterized by a non-linear film growth influenced by a three-fold augmentation in surface roughness and polarization effects. Notably, the surface morphology of the CNP films undergoes modification, exhibiting larger grains and a reduced optical band gap energy. Moreover, while maintaining a non-ohmic behaviour, the electric field plays a crucial role in increasing by about two orders of magnitude the electrical conductance of CNP films at ambient temperature. This effect is accompanied by a decrease in temperature sensitivity, attributed to the low and nearly temperature-independent activation energy for the tunneling of electrons in the percolative network. In summary, electric-field assisted deposition is a promising approach to tailor the thermal response of CNP films, which could be beneficial for the development of next-generation sensors.

1. Introduction

Over the past few years, there has been a growing interest in nanostructured films due to their potential applications in various fields, including energy, sensing, optoelectronics, and more. Carbon-based films are particularly advantageous as they are environmentally and health-friendly [1,2], making them ideal for medical applications or short-lifespan electrical and electronic devices [3]. Nanoparticle films offer the potential for use in the next generation of sensors due to their ability to conduct electricity. Such sensors need to be cost-effective, transparent, lightweight, easy to fabricate, biocompatible, and versatile, with flexibility being especially valuable. Currently, sensors based on nanoparticles (NPs) show great promise [4–9]. However, the electrical properties of these films are sensitive to thermal conditions in the environment, which can be a critical issue for practical applications [10–12]. To address this challenge, researchers have explored various approaches to tailor the temperature coefficient of resistance (*TCR*) of the sensing materials, to achieve zero or enhanced TCR [13]. A low-cost and straightforward method for producing carbon nanoparticles (CNPs) is the flame synthesis process.

Carbon particles formed in combustion are the result of a complex chemical and physical process occurring from any hydrocarbon fuel-rich combustion process [14–17]. As a byproduct of rich combustion processes, soot is mostly an unwanted material because it reduces combustion efficiency and because soot emissions in the atmosphere cause adverse environmental and health effects. However, soot can be also an engineered nanomaterial. The technological applications of soot, and in general of CNPs, have got significantly less attention from the scientific community than other well-known and thoroughly explored carbon-based nanomaterials such as fullerenes, carbon nanotubes, graphene, graphene oxides, and carbon-metal oxide composites [18–20]. Yet, soot has recently become increasingly common as a material for a variety of innovative uses [21], ranging from the production of hydrophobic coatings to their employment in a wide range of optical, electronic, and

* Corresponding authors.
E-mail addresses: gianluigi.defalco@unina.it (G. De Falco), mario.commodo@stems.cnr.it (M. Commodo).
[1] These authors contributed equally.

https://doi.org/10.1016/j.fuproc.2023.108027
Received 4 September 2023; Received in revised form 18 December 2023; Accepted 23 December 2023
Available online 30 December 2023

electrical devices, due to their chemical, structural, and morphological properties [3,22–24].

For a variety of practical applications, particles assembly into a uniform film with precise control of chemical and physical properties is required. Particularly interesting is the one-step procedure based on the flame synthesis of carbon nanoparticles and their direct deposition by thermophoresis. Indeed, this is a simple, one-step, reliable, and low-cost procedure that does not make use of solvents or toxic substances [25–27]. The films can be deposited on a variety of substrates with arbitrary shapes. In particular, the deposition on a substrate with interdigitated electrodes opens the exploitation of the CNP films in electronic applications [25–27]. These films are made of grains and voids, whose arrangement depends on the properties of the particles generated into the flame and the deposition time. De Falco et al. [28,29] investigated the morphology and conductivity of these films, showing that electrical conduction can be described as the tunneling of charge carriers between two neighboring particles in a percolative network. This results in non-ohmic conduction and high sensitivity to changes in environmental temperature [30]. This last feature, together with the mentioned advantages of the material microfabrication processing and biocompatibility of the carbon material, makes these films ideal for temperature sensing in many environments.

A further aspect of the flame reactor to be considered is that it is a weakly ionized plasma containing electrons, ions, and charged particles together with neutral species [31]. Therefore, the performance of flame reactors is sensible to the application of external electromagnetic fields. These aspects have been studied for several decades [32]. An extensive review of the ion chemistry in flames was reported by Fialkov in 1997 [33]. The primary effect of imposing electric fields on flames is the separation of charged species, which migrate toward the cathode and the anode according to the sign of their charge. Depending on the positioning of the cathode and anode in the flames, the application of the electric field leads to an increase or a reduction of CNP formation and growth [34]. In a former paper, we proposed a new electric field-assisted flame synthesis method for CNP film production [35]. This uses a specific setup to add a negative DC voltage to the substrate used for the thermophoretic deposition process. The electric field-assisted process significantly improves the deposition rate and the electric field in flame significantly alters the CNP deposition velocities and impact angles, as suggested by a model analysis [35].

The objective of this work is to shed light on the effect of the electric field on the optical and electrical properties of the nanostructured film produced by the electric field-assisted thermophoretic deposition. Specifically, we experimentally study the thermo-resistive response to develop a simple manufacturing methodology ideal for tailoring the optical and thermo-resistive properties of the films, particularly the temperature coefficient of resistance which can be useful for many practical advanced sensing applications [36–38].

2. Materials and methods

2.1. Experimental setup and operating conditions for CNP film deposition

A sketch of the complete setup for CNP film deposition is shown in Fig. 1. The experimental apparatus for CNP film production consisted of three main units: the flame reactor for CNP production, the Electrical Charging unit, and the sampling system.

CNP films were generated by a flat laminar premixed ethylene-air flame stabilized on a water-cooled McKenna burner. Ethylene has been chosen because it is largely used as a proxy for the combustion of aliphatic hydrocarbons. The McKenna burner– a widely utilized commercial reactor in combustion research– allows precise temperature, gas concentration, and particle concentration measurements over combustion time by selecting the probe volume at various height above the burner (*HAB*). Indeed, in such flat laminar premixed flames, the residence time is directly proportional to the height above the burner. To investigate the production of CNP films in slightly sooting conditions, the C/O ratio was set to 0.67 using an airflow rate of 13.06 L/min and an ethylene flow rate of 1.79 L/min, maintained *via* flow controller. Under these conditions, the cold gas velocity was 9.8 cm/s. The CNP size

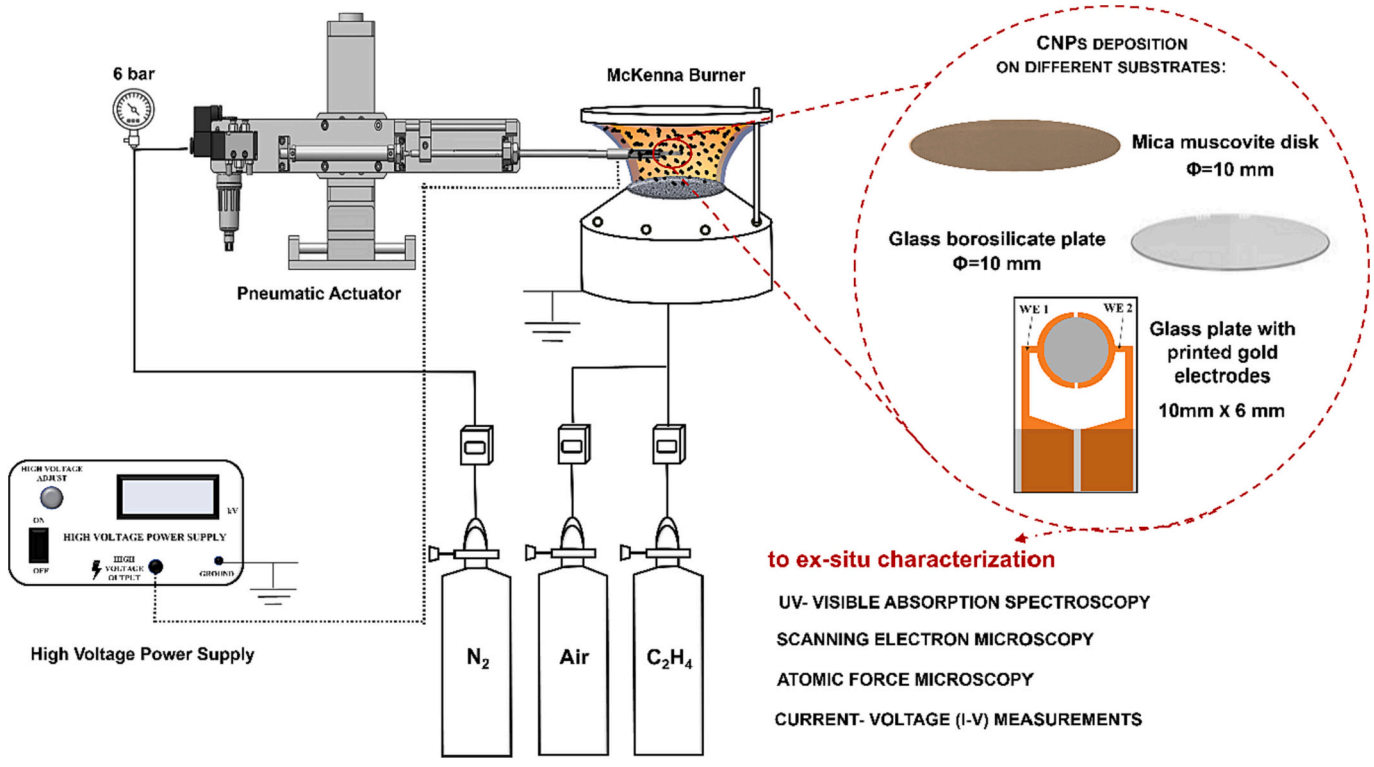

Fig. 1. Sketch of the electrophoretic-thermophoretic film deposition setup.

distribution in the flame is known from previous works [25,39–41]. It shows a typical bimodal shape with a first mode (Mode I in the following) around 2–3 nm and a second one (Mode II thereinafter) made by particles larger than 10 nm. Moreover, CNP charge distributions are also known from previous works that also reported an equal distribution of positively and negatively charged particles sampled from flames at atmospheric pressure and that all the particles with sizes up to 20 nm bear at most a single electric charge [42].

From previous works [26,40–42], it was well-known that flame synthesis is largely used to produce CNP films, primarily controlled by thermophoresis. However, thermophoretic deposition is characterized by a low harvesting rate, which is a relevant issue for the overall process productivity. A recently developed model [35] showed that the superimposition of an electric field to the flame can improve the deposition rate of CNPs, overcoming the rate limitations of conventional-thermophoretic driven flame synthesis. To implement this, a setup for electrophoretic-thermophoretic film deposition was devised, as depicted in Fig. 1.

A High Voltage Power Supply Spellmann model Bertan 230-20R with reversible polarity was used to generate and sustain the external electric field. The electric potential was applied directly to a CNP deposition substrate and inserted in flame at a fixed distance from the burner inlet, maintaining the burner grounded. In these conditions, the rapid insertion of the charged substrate into the flame had the potential to influence the dynamics of particle impacting with the substrate. However, it was expected that neither the flame behaviour nor the kinetics of nanoparticle growth inside the flame would be altered. The characteristic time of flame reactions is significantly shorter than the time of the electrical perturbation in flame and a steady-state condition for flame kinetics was achieved in the time required for a single fast insertion.

CNP films were deposited on different substrates (*see* Fig. 1). In particular, mica disks with a 0.251 mm thickness were used for surface analysis by Atomic Force Microscopy since it is a uniform and nearly flat surface, free of all strains, foreign inclusions, cracks, and other similar defects. Borosilicate glass disk with a thickness of 0.3 mm was used for optical characterization tests since it is a lightweight, low-cost inert substrate. In addition, sampling was performed with metal-based InterDigitated Electrodes (IDE) fabricated by thin-film technologies on a Glass substrate by MicruX Technologies, ED-IDE1-Au, shown in Fig. 1.

The sampling system consisted of a double-acting pneumatic cylinder fed with nitrogen at 6 bar equipped with a mobile extension arm, used to rapidly insert at a specific distance from the burner inlet– known as height above the burner (*HAB*)– a holder containing the deposition substrate to select and collect particle population. The insertion time, t_{ins}, was 100 ms, and *HAB* was 15 mm. The number of insertions in flame was varied to obtain CNP films with a different deposited mass. The probe containing the substrate was kept at a fixed electric potential V_0, while the burner was grounded. Preliminary experiments have been carried out to determine the onset potential for corona discharge in our setup. This value is close to −4 kV. Accordingly, during the CNP deposition experiments, the electric potential on the substrate was fixed at 0 kV and − 3 kV. Table 1 resumes all the explored experimental conditions.

Table 1
List of the explored experimental conditions.

Description (units)	Values
C/O ratio (−)	0.67
Air flow rate (L/min)	13.6
Ethylene flow rate (L/min)	1.79
Cold gas velocity (cm/s)	9.8
Sampling position *HAB* (mm)	15
Insertion time t_{ins} (ms)	100
Deposition substrates	Mica Muscovite Disk Borosilicate Glass Disk Metal InterDigitated electrodes
Applied voltage V_0 (kV)	0; −3
Number of insertions N_{ins} (−)	At 0 kV: from 100 to 600 At −3 kV: from 25 to 150

2.2. CNP film characterization

CNP films were analysed with different analytical techniques. UV–vis absorption measurements were performed on the CNP films deposited on glass substrates by an Agilent UV–vis 8453 spectrophotometer. For both electric voltages applied to the deposition substrate, samples with various numbers of insertions in flame were analysed to carry out structural characterization. For each sample, the UV–vis spectrum allowed the determination of Absorbance– Abs(λ)– at each wavelength (λ). This information provides qualitative insights into the deposited mass and enables quantitative estimations of CNP growth rate and optical film thickness using the Beer-Lambert Law [43].

Moreover, for semiconductor materials, the UV–vis spectrum can measure the optical band gap using Tauc's procedure [44]. This gap depends mainly on the different hybridization of the carbon atom wave functions, either sp^3 or sp^2, but also the size of the π-bonded clusters of sp^2 carbon atoms. Thus, the optical band gap is a powerful indicator of the nature of the carbonaceous structures produced in rich flames and provides a physical characterization of the final CNP films: A value closer to zero signifies a greater graphitic character of the material. Following Tauc's equation, the absorbance Abs can be expressed as a function of the optical band gap energy E_g:

$$Abs \bullet h\nu = \left(h\nu - E_g\right)^2 \quad (1)$$

Where h is Planck's constant; ν is the frequency of the incident light; n is a constant depending on the optical transition; E_g is the band gap.

In particular, the value of n in Tauc's equation can be equal to ½ or 2 for direct and indirect transitions, respectively. For CNPs in the explored conditions, it was verified that $n = 2$. Thus, the optical band gap energy can be estimated by plotting the square root of the first term of eq. (1) as a function of the $h\nu$ – the energy of the incident photon – and extrapolating the linear slope in this plot to zero absorption in a range of photon energy equal to 1.5–3.5 eV [45].

Moreover, Scanning Electron Microscopy (SEM, MODEL FEI Inspect S 50) was used to analyze the morphology of two different samples obtained at 0 and − 3 kV, which are characterized by the same amount of deposited material (same absorbance).

Atomic force microscopy (AFM) measurements were performed with a Scanning Probe Microscope NTEGRA Prima from NT-MDT, operated in a semi-contact mode in air and equipped with NANOSENSORS™ SSS-NCHR super-sharp silicon probes with a nominal tip radius of 2 nm. The AFM images provided information in terms of CNP sizes and spatial distribution on the substrate. In addition, the distribution of the heights, the average roughness on the nanoscale (S_a), and the maximum height (S_{max}) of the nanostructures was obtained.

For thermal and electrical analysis, the samples were placed in a Linkam HFS600E-PB4 heating stage with electrical probes and the T95 controller system. Current-voltage (*I-V*) curves were measured for the electrical characterization of CNP films using a Source Measure Unit (SMU) (type 200, from Ossila Ltd., Sheffield, UK) that simultaneously supplies voltage and measure current with high accuracy. Specifically, voltage sweeps were performed between −10 and 10 V with a step of 0.5 V and a voltage scan rate of 6.2 V/s.

3. Results and discussion

Fig. 2 shows the UV–vis absorption spectra of the CNP films produced varying the number of insertions, N_{ins}, of the substrate in the two flames with 0 and – 3 kV applied to the deposition substrate.

The light absorption spectra of CNPs show a decrease trend with wavelengths, *i.e.* moving from the UV to the visible spectral region. For a fixed electric potential, there is an upward shift in the absorption

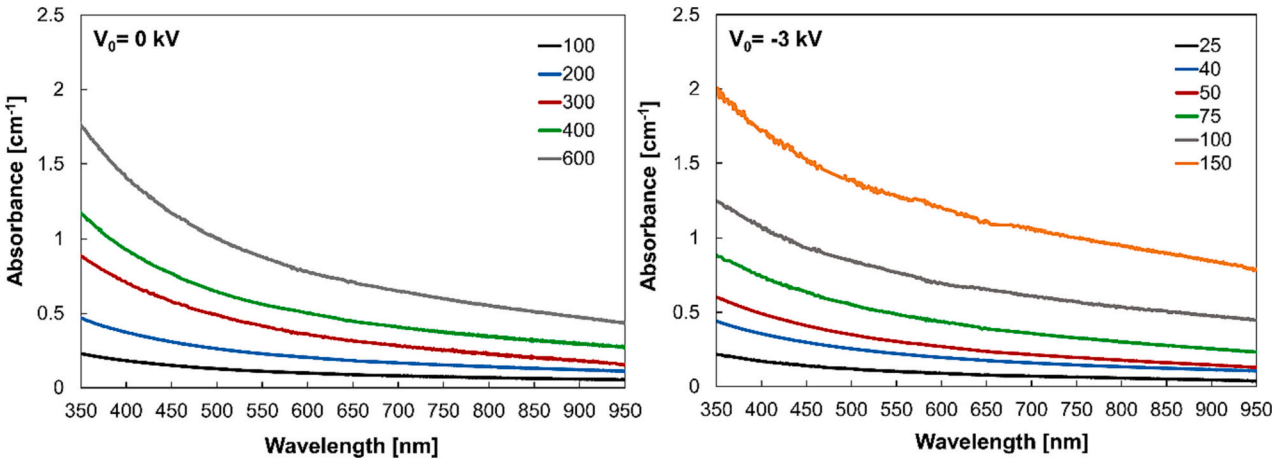

Fig. 2. UV–vis absorption spectra of the CNP films collected in the flame (C/O = 0.67; *HAB* = 15 mm; t_{ins} = 100 ms) for the electric voltage applied to the deposition substrate, V_0, equal to 0 kV (left) and − 3 kV (right) and varying the number of insertions, N_{ins}, in flame. 0 kV: N_{ins} from 100 to 600; −3 kV: N_{ins} from 25 to 150.

spectrum as the number of insertions in flame increases. This shift is a consequence of the increase in the film thickness and so of an increase in the deposited mass of material on the substrate. We showed in previous works that for thin films of flame-formed CNPs the chemical/structural composition of the films does not change with the film thickness. The grains inside the film consist of small graphitic crystallites with constant size. Also, other properties of the films, such as the electrical conductivity, follow a well-defined trend as a function of the film thickness, rapidly increasing for low thickness range and then mild decaying for higher thicknesses [29].

Moreover, for a fixed number of insertions in flame, there is an increase in the absorbance when the electric potential goes from 0 to – 3 kV.

To better evaluate the effects of the electric voltage on the absorbance, it is possible to show how the absorbance at a fixed wavelength varies with the number of insertions and with the electric voltage applied to the deposition substrate (Fig. 3A). A reference wavelength of 532 nm is selected since this is often considered in the evaluation of soot mass [46].

From Fig. 3A it is possible to notice that for an electric potential equal to 0 kV there is a linear increase of the absorbance with the number of insertions. The slope of the linear fit is 0.001 and it represents the amount of particle deposition per insertion. Such a linear dependence of absorbance as a function of the number of insertions indicates that, within the experimental range explored here, the thermophoretic deposition yield is not strongly affected by the film formation, but mostly relies on the collisional mechanism. This result is consistent with those predicted by the harvesting model shown in our recent work [35]. However, at −3 kV the measurements show that a power law, characterized by a constant equal to 0.002 and an exponent of the power law equal to 1.35, better represents the trend, showing that the film growing is the controlling mechanism, which determines an enhancement on the particle collection efficiency. To further clarify this aspect, Fig. 3B shows the film absorbance normalized to the number of insertions as a function of the number of insertions.

From Fig. 3B, it is possible to notice that at 0 kV the CNP film absorbance normalized to the number of insertions is almost constant. On the other hand, at −3 kV there is a strong nonlinear increase. As the electric potential is applied to the deposition substrate, more and more material is collected as the number of insertions increases. This suggests that the CNP deposition rate is influenced by the film thickness growth. From a deeper analysis of Fig. 2, it is possible to notice that the decrease from the UV to the visible spectral range becomes less pronounced with an applied voltage. To better quantify this change, Fig. 4 shows the light absorption measured at the fixed wavelength of 800 nm *versus* the light absorption measured at the fixed wavelength of 400 nm for all the samples collected varying the number of insertions at 0 and − 3 kV.

The data for the samples deposited with 0 kV follow a single straight

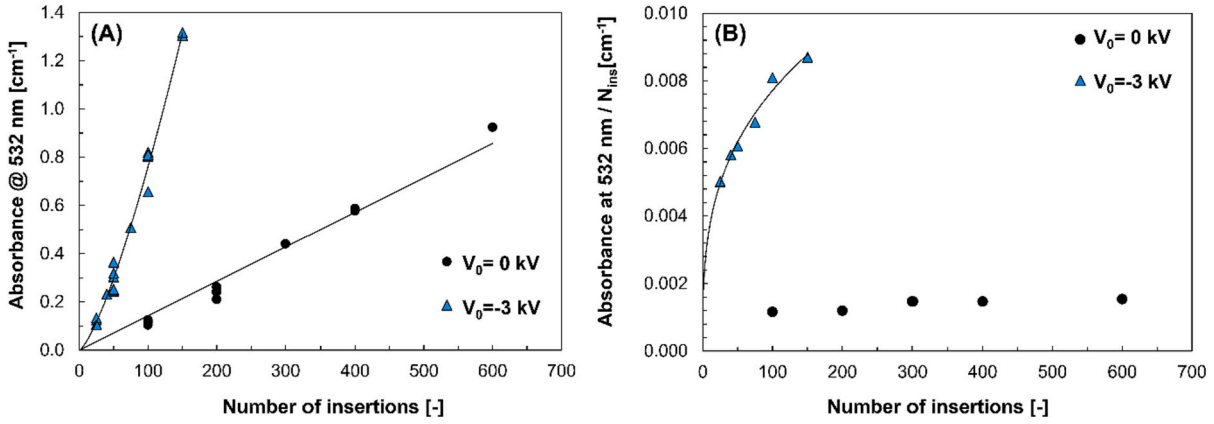

Fig. 3. (A) Absorbance at 532 nm ($Abs_{532\ nm}$) as a function of the number of insertions (N_{ins}) for the two electric voltages applied to the deposition substrate. (B) CNP film absorbance at 532 nm normalized to the number of insertions as a function of the number of insertions for an electric potential equal to 0 kV (black dots) and – 3 kV (blue triangles). The results of the best fit of the data are also shown: At V_0 = 0 kV the best fitting is linear (equation $Abs_{532nm} = 0.001*N_{ins}$; $R^2 = 0.99$); at V_0 = −3 kV the best fitting is a power law (equation $Abs_{532nm} = 0.002*N_{ins}^{1.349}$; $R^2 = 0.99$). (For interpretation of the references to colour in this figure legend, the reader is referred to the web version of this article.)

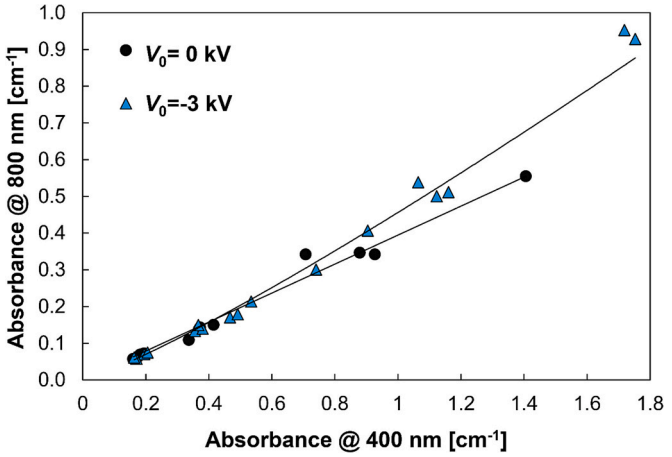

Fig. 4. Light absorption of the flame-formed CNPs at 800 nm as a function of the absorption at 400 nm measured in samples collected for different numbers of insertions in the flame at 0 kV (black dots) and − 3 kV (blue triangles). The best fit (with $R^2 = 0.99$) of 0 kV and – 3 kV (black lines) is also reported. (For interpretation of the references to colour in this figure legend, the reader is referred to the web version of this article.)

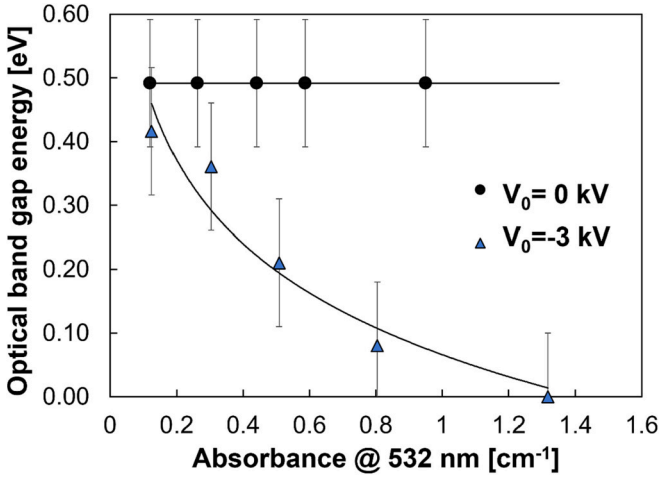

Fig. 5. Optical band gap energy as a function of the absorbance at $V_0 = 0$ kV (black dots) and $V_0 = -3$ kV (blue triangles). Error bars are reported. (For interpretation of the references to colour in this figure legend, the reader is referred to the web version of this article.)

line with slope 0.39, indicating that the absorbance at both wavelengths increases at the same rate as the film thickens, the absorption spectra do not change and thus the film retains the same composition. By contrast, at −3 kV two regions can be observed: in the first region, for lower absorbance values, *i.e.* thinner films, one can observe the same trend as the case of 0 kV samples. However, when the absorbance at 400 nm becomes higher than nearly 0.5 cm^{-1}, a different trend can be observed. Overall, the best fit at −3 kV is a power law with a constant equal to 0.46 and an exponent equal to 1.16. To analyze this behaviour, we can consider that the size distribution of the particles in the selected flame condition is bimodal. As shown in previous works [39,47], it consists of a Mode I of small particles with sizes of about 1.5–2 nm and a Mode II of larger particles, from 3 to 15 nm with an average size of 8 nm. Particles in the first mode are characterized by an absorption spectrum high in the UV and strongly decreasing toward the visible, the particle band gap is larger than 1 eV so that these particles absorb UV light (400 nm) but are rather transparent to the infrared (800 nm). The particles in the second mode are characterized by an absorption spectrum high in the UV that slowly decreases toward the infrared, consistently with a band gap of a few tens of eV [41,47]. Considering this, the light absorption in the UV-blue spectral region, and thus the absorbance at 400 nm, is representative of both classes of particles while the light absorption measured in the NIR region, and thus at 800 nm, is only representative of the larger particles. The non-linear trend observed in Fig. 4 for the sample produced with electrophoretic harvesting suggest that, as the film is sufficiently thin, a similar particle population is collected as in the case of 0 kV, whereas, in thicker samples, larger particles (Mode II) are collected more efficiently as indicated by the larger absorbance measured in NIR with respect to the UV. Such a preferential deposition of larger particles is further supported by a larger collisional efficiency predicted in a previous paper [31].

Fig. 5 shows the optical band gas as a function of the CNP film absorbance at 532 nm at 0 and − 3 kV, estimated following the procedure described in the previous section.

It is possible to notice that at $V_0 = 0$ kV the optical band gap remains almost constant as the absorbance – the amount of deposited mass – increases. The value is equal to 0.5 ± 0.1 eV [47].

On the contrary, the CNP films obtained in the presence of electrical potential show a different trend, with a marked reduction in the optical band gap, from 0.5 ± 0.1 eV to 0 ± 0.1 eV as the absorbance increases. The optical band gap reduction may be presumably linked to the higher collisional efficiency of larger (Mode II), charged, soot particles, which have a more graphitic composition [31]. However, we cannot exclude that, due to the relatively low fraction of charged particles in the flame, this effect seems not completely consistent with the observations, and we envisage that the optical band gap reduction may be related also to a different morphology of the film. Indeed, film thickness and surface structure have been found to affect the energy band gaps of porous thin films [8,12,45].

SEM measurements were performed on the samples to analyze their morphologies. Fig. 6 shows the SEM images on the samples with $V_0 = 0$ kV and $V_0 = -3$ kV. From Fig. 6a, it is possible to observe that the sample with −3 kV potential has bigger clusters. These clusters are presented also in the zoom area (Fig. 6b). Whereas the film deposited with $V_0 = 0$ kV is more uniform and does not show any big cluster in it.

An AFM analysis has also been performed on two samples deposited on mica substrates, namely a CNP film collected with $V_0 = 0$ kV and $N_{ins} = 400$ and a CNP film collected with $V_0 = -3$ kV and $N_{ins} = 100$. The two samples are characterized by similar absorbance and thus similar amounts of deposited CNPs. Fig. 7 reports typical AFM images measured over an area of 2 mm × 2 mm of the CNP films visualized both in 2D and 3D mode, together with the distribution of the heights and some statistical parameters obtained from the AFM images.

Both samples are continuous granular films composed of nanoscale grains. The maximum height of the film collected with $V_0 = -3$ kV is about four times larger than the maximum height of the film collected with $V_0 = 0$ kV. In addition, the film deposited with an electric voltage of −3 kV is characterized by deeper voids and larger grain size with respect to the film deposited at 0 kV. This is evidenced by the surface roughness of the samples obtained by measuring the average roughness from the distribution of heights. The average roughness increases from 4.5 nm for the $V_0 = 0$ kV sample to 14 nm for the $V_0 = -3$ kV CNP film sample. In previous work on thermophoretic deposition [25], a deviation from a pure ballistic process and a large increase of roughness with the deposition time was observed and ascribed to preferential deposition of landing particles on the already deposited particles and/or diffusion and coagulation of particles after landing. The enhancement of this effect is here observed as produced by the applied electric field. This can be explained either by the microscale fluctuations of the electric field produced by the substrate and by the CNP film roughness, and by polarization effects that are likely to favour the formation of particle stacks. This effect was also shown in the AFM images for a single insertion in flame reported in [31].

Both effects may determine faster deposition that takes place preferentially over the already deposited particles due to the higher

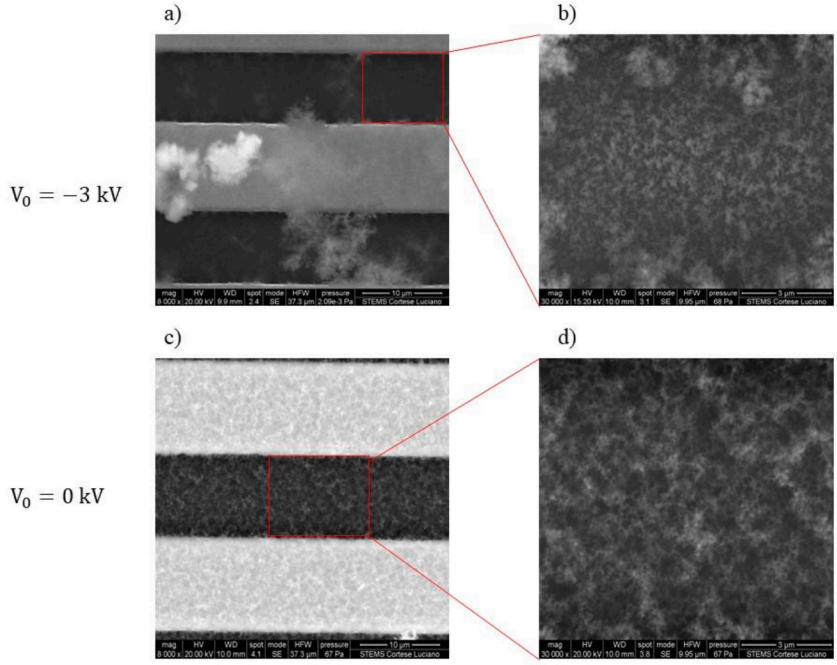

Fig. 6. SEM image for film deposited with $V_0 = -3$ kV and $N_{ins} = 100$ (a) and magnification (b). SEM image for film deposited with $V_0 = 0$ kV and $N_{ins} = 400$ (c) and magnification (d).

chemical affinity [13,14] and preferential deposition of the larger particles that, having a larger refractive index [48], also have larger polarizability [31].

These effects justify the strong non-linear increase of light absorbance and the change of spectral shape produced by the applied voltage shown in Figs. 3–4.

The electrical properties of the samples were investigated by measuring the current-voltage characteristics (*I-V*) of the CNP films deposited with the two values of the electric field, *i.e.* 0 kV and − 3 kV. The number of insertions was selected to deposit a similar amount of material in all the samples. The *I-V* curves were measured in the voltage range − 10 V to 10 V. As can be seen in Fig. 8, both curves are symmetric and non-linear, a trend that is characteristic of non-ohmic behaviors. The conductance of the samples is defined as the slope of the *I-V* curve over a linear range. According to Fig. 8, the conductance was calculated in the voltage range of 9 to 10 V. The slopes of the curves indicate that the sample at −3 kV has a conductance of about two orders of magnitude higher than that at 0 kV.

In this type of material, the local electrical conduction can be explained by tunneling (transferring) of electrons from one grain to the neighboring grains in a percolative network [25,26]. This assumption led Bruschi and Nannini to derive the theoretical equation shown below, which determines the bulk *I-V* characteristic of a granular material whose electrical conduction is controlled by percolation and tunneling between grains [49,50]:

$$I = C\left[\frac{A - BV}{exp\left(\frac{A-BV}{T}\right) - 1} - \frac{A + BV}{exp\left(\frac{A+BV}{T}\right) - 1}\right] \quad (2)$$

where the coefficient A is associated with the activation energy of the process E_{act} by $A = E_{act}/K_B$ with K_B the Boltzmann constant. The coefficient B is a constant dependent on both temperature and kind of material. The coefficient C depends on the so-called tunneling distance, S, being $C \propto \exp.(-S)$.

In this model, the transfer of electrons from one grain to another, separated by the tunneling distance, was linked to a change in the electrostatic energy of the pair of particles, E_{act}, which can be assumed to be the activation energy of the process [49,50].

The activation energy and the parameter C can be calculated by fitting the experimental data (*I-V* curves) into the Bruschi and Nannini models. Here, for the sample with $V_0 = 0$, $E_{act} = 51 \pm 2$ meV and $\ln(C) = -19.9 \pm 0.1$ A/K. The corresponding values for the film deposited with potential $V_0 = -3$ kV are $E_{act} = 44 \pm 9$ meV for and $\ln(C) = 14.9 \pm 0.5$ A/K. The larger current flowing through the film formed under electrophoretic harvesting with $V_0 = -3$KV with respect to that produced by pure thermophoresis, $V_0 = 0$ KV, sample is due to the C parameter that is two orders of magnitude larger. This is reflected in a lower tunneling distance while the activation energy, *e.g.* the nature of the grains, is similar.

The next step was to determine the sensitivity of our samples to temperature. To check this, we performed the *I-V* measurement in the temperature range from 298 to 373 K. All samples showed a reproducible pattern when measured on different days. Fig. 9 reports the response of our samples to the mentioned temperature range. As can be seen, increasing the applied voltage from 0 to −3 kV leads to a reduction in the temperature sensitivity, and eventually, the sample with 100 insertions and $V_0 = -3$ kV shows almost no sensitivity to the temperature change. Differently, the conductivity of the thermophoretically deposited films at 0 kV samples increases by increasing the temperature from 298 K to 373 K.

This increase proves that CNPs conductivity is a thermally assisted process, which agrees with the presence of an energy barrier between the particles [30]. Fig. 10 reports the conductance of the samples, G, in μS, as well as its dependence on the inverse of the absolute temperature, T.

In terms of absolute values, the conductance of the −3 kV sample is more than 10 times higher than that observed for the 0 kV samples. For both samples, the plot of the logarithm of conductance as a function of $1/KT$ shows a linear trend whose slope is an indication of the thermal activation energy (based on Arrhenius plot) for the electrical conduction, E_a. This quantity is highest for the film deposited with a potential of 0 kV, $E_a = 166 \pm 5$ meV, and it is one order of magnitude lower, $E_a = 10 \pm 1$ meV, for the film deposited with a potential of −3 kV. Based on the

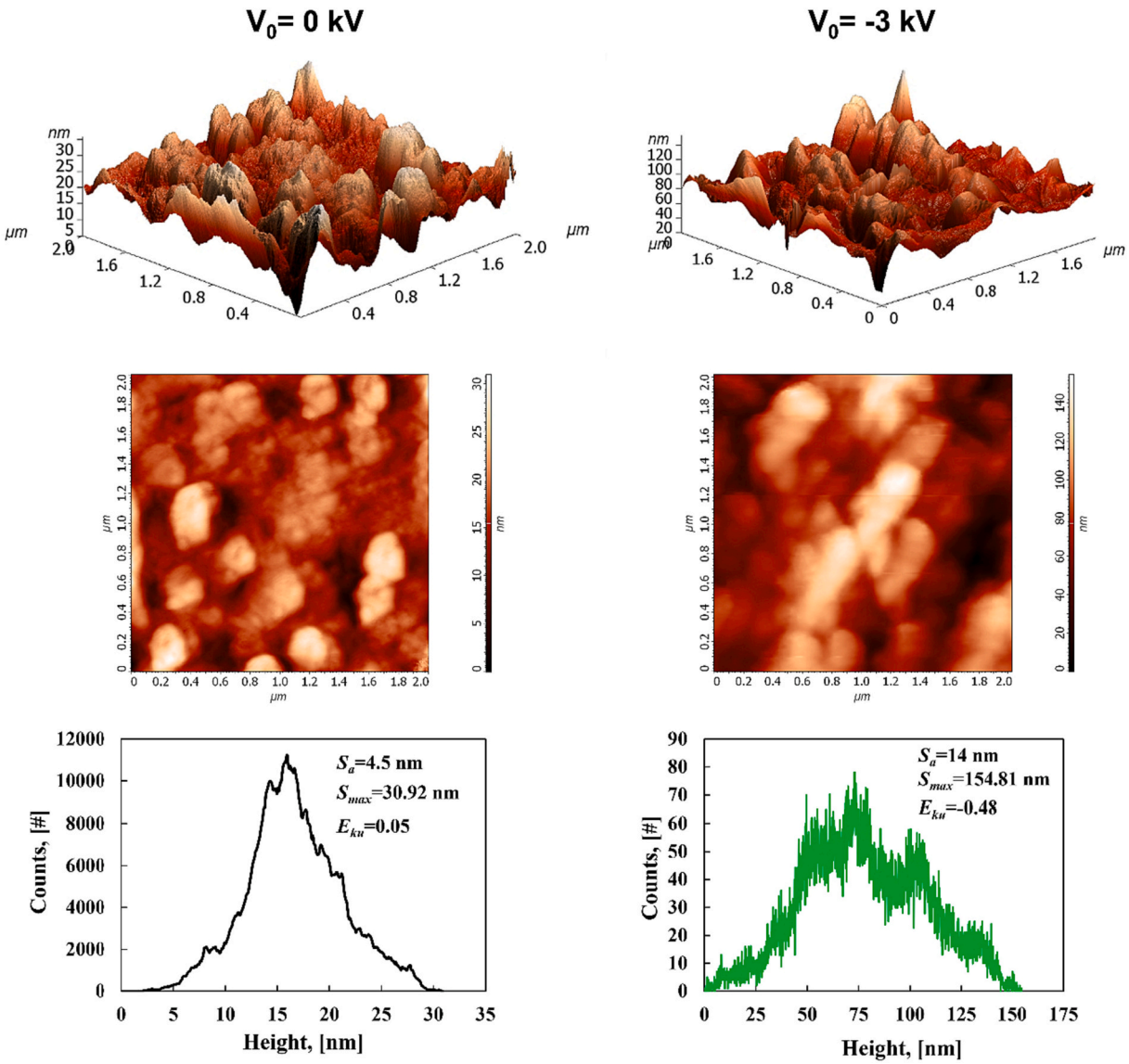

Fig. 7. From top to bottom: AFM 3D and 2D images and distribution of the heights for CNP films deposited at $V_0 = 0$ kV and $N_{ins} = 400$, z-axis scale range 0–30 nm (*left*) and CNP thin film deposited at $V_0 = -3$ kV and $N_{ins} = 100$, z-axis scale range 0–120 nm (*right*). The values of average roughness (S_a), maximum height (S_{max}) and excess kurtosis (E_{Ku}) are reported.

film characterization previously discussed, we can assume that the larger amount of small particles of organic nature, *i.e.*, with high hydrogen-to-carbon ratio, in the film deposited without applying an electric field hinders the flow of free electrons among the film, producing an energy barrier similar to the case of conductive particles dispersed in an insulating matrix. This would explain the non-linearity of the curves and temperature dependence. The lower amount of these particles deposited when the electric field is applied makes it easier for electrons to flow within the film so that the non-linearity of the *I-V* curve decreases, and they become rather independent of temperature. This can be also confirmed by applying the Bruschi and Nannini model [49,50]. Table 2 presents the results obtained from this fitting at 298 and 373 K.

As we can see from Table 2, activation energy does not depend on temperature. The difference between the activation energies at two temperatures, *i.e.* 298 and 373 K, stays within the error bars for both samples. Different is the case of ln(*C*), which is rather constant with *T* for the $V_0 = -3$ KV sample while is sensibly smaller at a larger temperature for the $V_0 = 0$ KV sample.

The fact that Arrhenius' theory examines the effects of temperature on the sample at a fixed voltage while Bruschi and Nannini's equation is based on varying the voltage while keeping the temperature constant can explain the difference between the activation energies based on the two theories (Arrhenius and Bruschi and Nannini). Since they consider two different processes, the observed difference may be reasonable. A similar result was found by Bruschi and Nannini in their papers [49,50] where the activation energy estimated based on their theory and Arrhenius's theory was found to be in the same order of magnitude. The difference observed for ln (*C*) is consistent with the larger number of small particles of organic nature mixed with the more graphitic larger particles in the film sampled without an applied potential that is probably responsible for a larger tunneling distance experienced by the electrons as they flow within the film.

Two important parameters for possible applications are the temperature sensitivity, *TS*, and the temperature coefficient of resistance (*TCR*).

TS is defined as:

$$TS = \frac{I_{373} - I_{298}}{I_{298}} \tag{3}$$

Where I_{373} and I_{298} represent the current values at $V = 10$ V

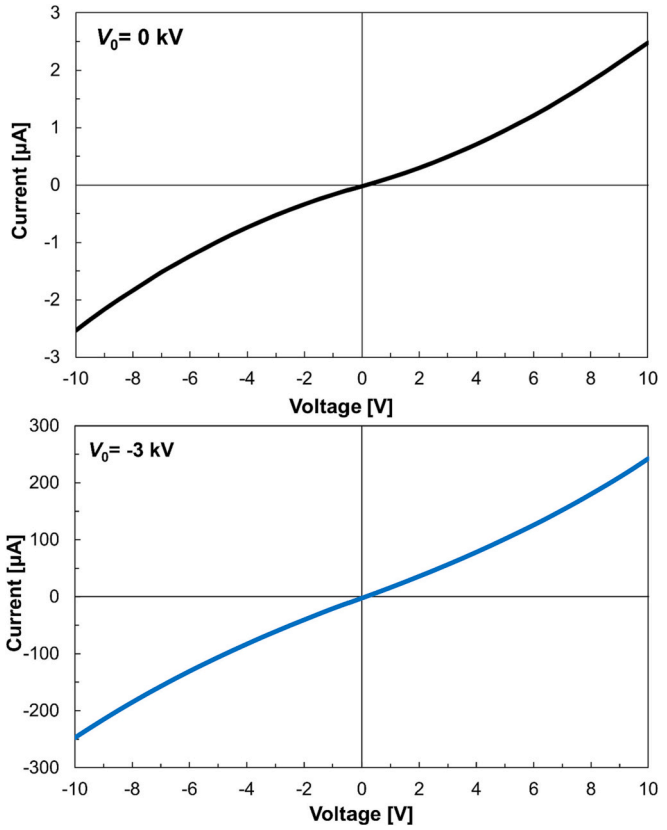

Fig. 8. *I-V* curves for collected CNP samples with applied voltages from 0 kV (upper panel) to −3 kV (bottom panel).

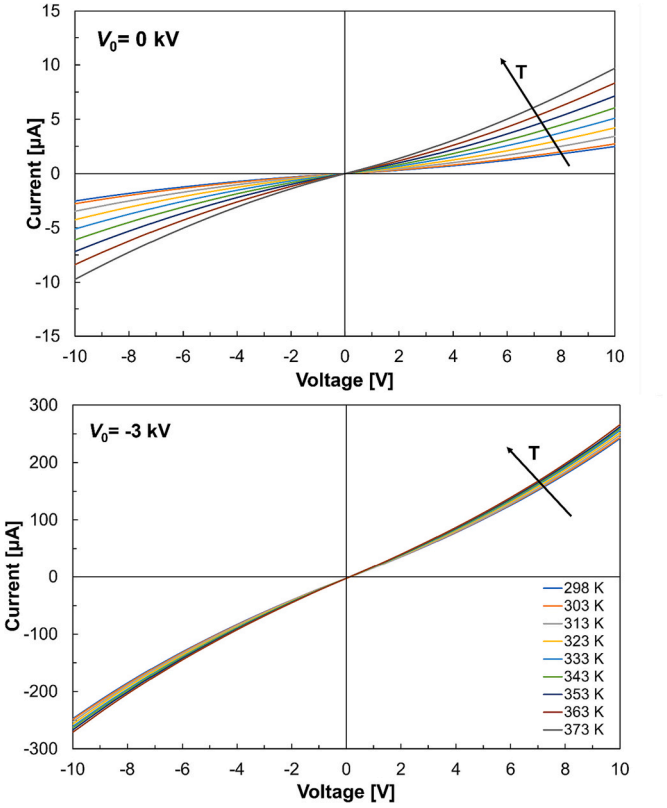

Fig. 9. The *I-V* curve variation with the increase of temperature for the CNPs samples collected at 0 kV and − 3 kV. Increasing the temperature results in a higher value for the current.

measured at 373 K and 298 K, respectively. The *TS* values at 0 kV and − 3 kV are reported in Table 3.

The temperature coefficient of resistance (*TCR*) is defined as:

$$TCR = \frac{1}{R}\frac{dR}{dT} \tag{4}$$

where *R* is the electrical resistance. The *TCR*, which is usually employed for the characterization of temperature sensors, is evaluated by the slope of the linear fit of ln(*R*) *versus T*. Because of the non-ohmic behaviour of the films, *R* was evaluated from the *I-V* curve either in the voltage ranges of [−1,1] or [9,10] (Table 3). Effectively tailoring the *TCR* is critical for composites with sensing capability. The thermal effect has become one of the most critical issues for the practical application of nanocomposite sensors and approaches to effectively tailor the *TCR*, including zero and/or enhanced *TCR*, have been developed [13].

The value for *TS* decreases almost 40 times, from 4.56 ± 0.04 to 0.110 ± 0.001 by increasing the potential from 0 to −3 kV. The same trend is valid for *TCR* evaluated in different voltage ranges. It drops from $-0.022 \pm 0.003\ K^{-1}$ to $-0.001 \pm 0.00015\ K^{-1}$ in the voltage range [9 V, 10 V] and reduce from $-0.026 \pm 0.003\ K^{-1}$ to $-0.0019 \pm 0.00023\ K^{-1}$ in [-1 V,1 V] range.

The use of an electric field-assisted particle deposition allows for tailoring the thermal response of the film. Films with high negative *TCR* or near zero *TCR* can be produced by simply changing the applied electric field during particle deposition. This film manufacturing procedure could be beneficial for the development of advanced sensing materials.

4. Conclusions

In this work, we reported a one-step process for nanostructured carbon film production, which is based on flame synthesis for CNP coupled with electric field-assisted thermophoretic CNP deposition. The results indicate that the presence of an electric field leads to a higher and non-linear film growth rate. Furthermore, UV–vis Absorption analysis suggested the preferential deposition of larger CNPs, *i.e.* those belonging to the II Mode of the Particle Size Distribution, is favoured. Compared to thermophoresis alone, the optical analysis revealed that the CNP films deposited in the presence of electric fields exhibit a reduced and almost zero optical band gap energy.

The electric field also affects film morphology. The AFM and SEM images showed that the presence of an electric field caused the maximum height on the CNP film to increase by four-times, and the presence of deeper voids and larger grains to appear, the average roughness to increase by three-times, going from 4.5 nm at 0 kV to 14 nm at −3 kV.

Electrical characterization revealed a non-ohmic behaviour for both samples, with and without applied electric field. On the other hand, the sample at V_0 = -3 kV was characterized by two-orders of magnitude higher conductance at ambient temperature. Additionally, the thermal sensitivity of the samples was decreased when an electric field was present during CNP deposition, the temperature coefficient of resistance decreasing by one order of magnitude when the applied voltage was V_0 = −3 kV. These findings support the idea that the thermal response of CNP films can be optimally tailored by utilizing the electric field during flame synthesis. This work demonstrates that the flame synthesis for CNP coupled with electric field-assisted thermophoretic CNP deposition is a promising process that allows easy tuning of the optical, morphological, and electrical properties of the produced nanostructured carbon film. Particularly relevant is the possibility of tailoring the sensitivity to the environmental temperature by simply modifying the voltage applied to the particle deposition line. This method could be helpful for the creation of cutting-edge materials for sensing applications.

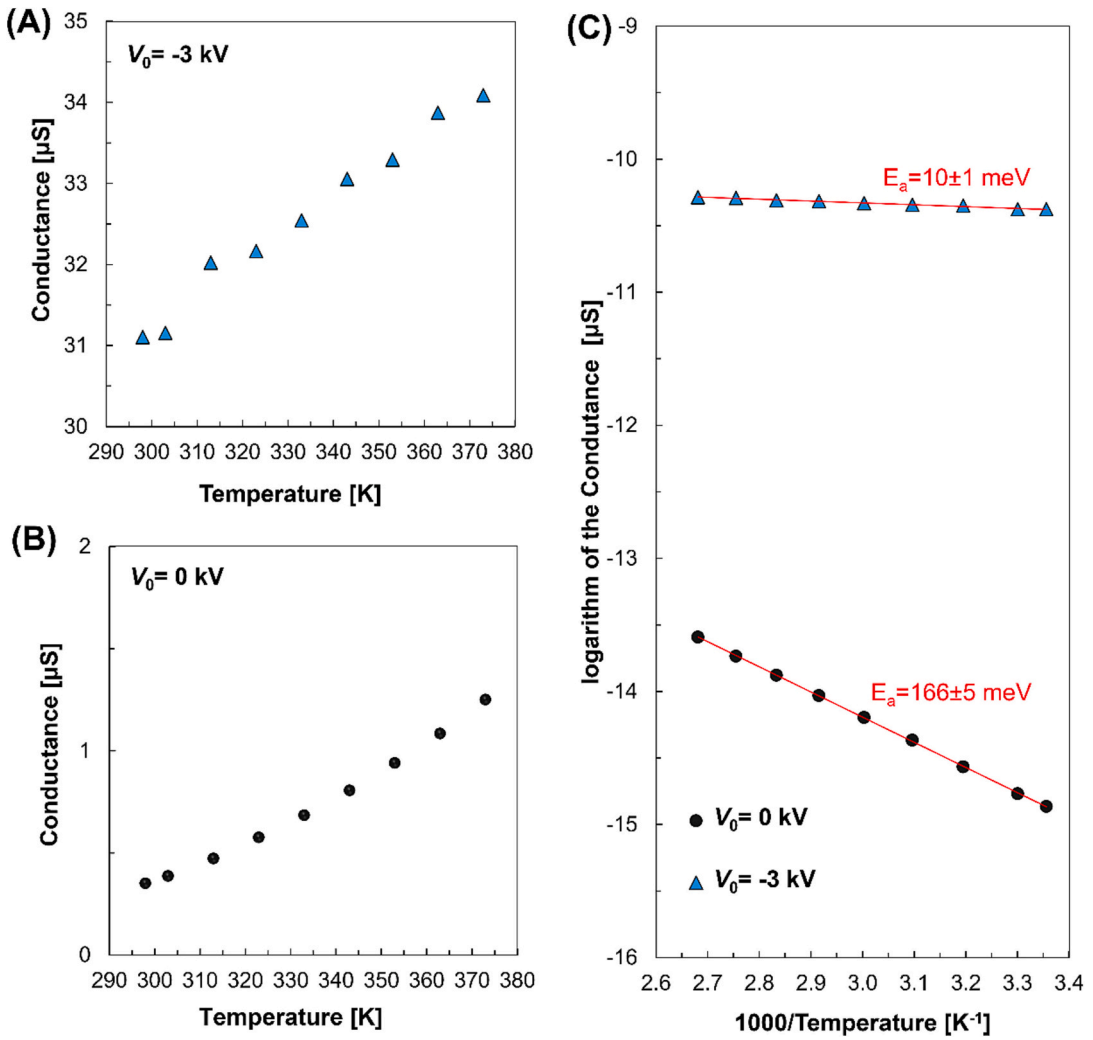

Fig. 10. Sample conductance in the potential range 9–10 V as a function of temperature; CNP thin film sampled at 0 kV (**A**), CNP thin film sampled at −3 kV (**B**). The Arrhenius plot showing the calculated activation energies of the two films (**C**).

Table 2
Activation energy, E_{act}, and parameter ln(C) (proportional to tunneling distance) calculated based on Bruschi and Nannini's theory [39,40].

Sample →	Temperature, K	$V_0 = 0$ kV	$V_0 = -3$ kV
E_{act}	298	51 ± 2 meV	44 ± 9 meV
	373	49.9 ± 0.6 meV	51 ± 13 meV
ln(C)	298	−19.9 ± 0.1 A/K	−14.9 ± 0.5 A/K
	373	−18.90 ± 0.04 A/K	−15.0 ± 0.6 A/K

Table 3
The sensitivity of samples to temperature increase, *TS*, and the temperature coefficient of resistance, *TCR*, evaluated from resistance in the voltage ranges of [−1,1] and [9,10].

Sample →	$V_0 = 0$ kV	$V_0 = -3$ kV
TS	4.54 ± 0.04	0.110 ± 0.001
$TCR_{[9\ V,10\ V]}$, K^{-1}	−0.022 ± 0.003	−0.001 ± 0.00015
$TCR_{[-1\ V,1\ V]}$, K^{-1}	−0.026 ± 0.003	−0.0019 ± 0.00023

List of symbols and abbreviations

A	Coefficient associated to the activation energy dependence in Bruschi and Nannini model (*K*)
Abs	Absorbance value (cm^{-1})
B	Coefficient associated to temperature and material dependence in Bruschi and Nannini model ($K{\cdot}V^{-1}$)
C	Proportionality coefficient in Bruschi and Nannini model ($A{\cdot}K^{-1}$)
CNP	Carbon NanoParticle (–)
C/O	Carbon-to-Oxygen Ratio (–)
E_{act}	Activation energy for electrical conduction (*meV*)
E_g	Optical band gap energy (*eV*)
E_{Ku}	Excess kurtosis (–)
G	Electrical conductance (*S, µS*)
h	Plank's constant ($J{\cdot}s$)
HAB	Height above the burner (*mm*)
I	Current (*µA, A*)
k(λ)	Imaginary part of the CNP refractive index (–)
N_{ins}	Number of insertions (–)
NP	NanoParticle (–)
ν	Frequency of the incident light (s^{-1})
R	Electrical resistance (Ω)
S_a	Average roughness (*nm*)
S_{max}	Maximum height of the CNP film (*Nm*)
T	Absolute temperature (*K*)
TS	Temperature sensitivity (–)
TCR	Temperature coefficient of resistance (K^{-1})
V	Voltage (*V*)
V_0	Applied voltage/ electric potential (*kV*)

t_{ins} Insertion time (*ms*)

CRediT authorship contribution statement

A. Parisi: Writing – original draft, Visualization, Methodology, Investigation, Formal analysis. **P. Darvehi:** Writing – original draft, Visualization, Methodology, Investigation, Formal analysis. **G. De Falco:** Writing – original draft, Visualization, Methodology, Investigation, Formal analysis, Conceptualization. **M. Sirignano:** Writing – review & editing, Visualization, Formal analysis. **M. Commodo:** Writing – review & editing, Visualization, Supervision, Methodology, Formal analysis, Conceptualization. **F. Di Natale:** Writing – review & editing, Supervision, Resources, Project administration, Funding acquisition, Formal analysis, Conceptualization. **P. Minutolo:** Writing – review & editing, Visualization, Supervision, Resources, Project administration, Funding acquisition, Formal analysis, Conceptualization.

Declaration of Competing Interest

The authors declare that they have no known competing financial interests or personal relationships that could have appeared to influence the work reported in this paper.

Data availability

Data will be made available on request.

Acknowledgements

The authors would like to thank Luciano Cortese for his help in performing SEM measurements. This work was financially supported by the PRIN project 2017PJ5XXX: “MAGIC DUST”.

References

[1] G. Landi, L. La Notte, A.L. Palma, A. Sorrentino, M.G. Maglione, G. Puglisi, A comparative evaluation of sustainable binders for environmentally friendly carbon-based supercapacitors, Nanomaterials 12 (2021) 46, https://doi.org/10.3390/nano12010046.

[2] J. Wang, H. Kong, J. Zhang, Y. Hao, Z. Shao, F. Ciucci, Carbon-based electrocatalysts for sustainable energy applications, Prog. Mater. Sci. 116 (2021), 100717, https://doi.org/10.1016/J.PMATSCI.2020.100717.

[3] R. Sanjinés, M.D. Abad, Vâju Cr, R. Smajda, M. Mionić, A. Magrez, Electrical properties and applications of carbon based nanocomposite materials: an overview, Surf. Coat. Technol. 206 (2011) 727–733, https://doi.org/10.1016/j.surfcoat.2011.01.025.

[4] L. Yuan, J. Dai, X. Fan, T. Song, Y.T. Tao, K. Wang, et al., Self-cleaning flexible infrared nanosensor based on carbon nanoparticles, ACS Nano 5 (2011) 4007–4013, https://doi.org/10.1021/nn200571q.

[5] E.T. Thostenson, T.-W. Chou, Carbon nanotube networks: sensing of distributed strain and damage for life prediction and self healing, Adv. Mater. 18 (2006) 2837–2841, https://doi.org/10.1002/adma.200600977.

[6] D.J. Lipomi, M. Vosgueritchian, B.C.-K. Tee, S.L. Hellstrom, J.A. Lee, C.H. Fox, et al., Skin-like pressure and strain sensors based on transparent elastic films of carbon nanotubes, Nat. Nanotechnol. 6 (2011) 788–792, https://doi.org/10.1038/nnano.2011.184.

[7] M. Segev-Bar, H. Haick, Flexible sensors based on nanoparticles, ACS Nano 7 (2013) 8366–8378, https://doi.org/10.1021/nn402728g.

[8] M. Ahmadipour, S.N. Ayub, M.F. Ain, Z.A. Ahmad, Structural, surface morphology and optical properties of sputter-coated CaCu 3 Ti 4 O 12 thin film: influence of RF magnetron sputtering power, Mater. Sci. Semicond. Process. 66 (2017) 157–161, https://doi.org/10.1016/j.mssp.2017.04.019.

[9] M. Ahmadipour, M. Arjmand, Qurratu Aini Abd Aziz, SN, Chiam SL, Ahmad ZA, Pung S-Y., Influence of annealing temperature on morphological and photocatalytic activity of sputter-coated CaCu3Ti4O12 thin film under ultraviolet light irradiation, Ceram. Int. 45 (2019) 20697–20703, https://doi.org/10.1016/j.ceramint.2019.07.053.

[10] R. Kumar, E. Joanni, R.K. Singh, D.P. Singh, S.A. Moshkalev, Recent advances in the synthesis and modification of carbon-based 2D materials for application in energy conversion and storage, Prog. Energy Combust. Sci. 67 (2018) 115–157, https://doi.org/10.1016/j.pecs.2018.03.001.

[11] P. Joshi, R. Mishra, R.J. Narayan, Biosensing applications of carbon-based materials, Curr. Opin. Biomed. Eng. 18 (2021), 100274, https://doi.org/10.1016/j.cobme.2021.100274.

[12] M. Ahmadipour, M.F. Ain, Z.A. Ahmad, Effects of annealing temperature on the structural, morphology, optical properties and resistivity of sputtered CCTO thin film, J. Mater. Sci. Mater. Electron. 28 (2017) 12458–12466, https://doi.org/10.1007/s10854-017-7067-3.

[13] S. Gong, Z.H. Zhu, Z. Li, Electron tunnelling and hopping effects on the temperature coefficient of resistance of carbon nanotube/polymer nanocomposites, Phys. Chem. Chem. Phys. 19 (2017) 5113–5120, https://doi.org/10.1039/C6CP08115K.

[14] H.A. Michelsen, M.B. Colket, P.-E. Bengtsson, A. D'Anna, P. Desgroux, B.S. Haynes, et al., A review of terminology used to describe soot formation and evolution under combustion and pyrolytic conditions, ACS Nano 14 (2020) 12470–12490, https://doi.org/10.1021/acsnano.0c06226.

[15] J.W. Martin, M. Salamanca, M. Kraft, Soot inception: Carbonaceous nanoparticle formation in flames: soot inception, Prog. Energy Combust. Sci. (2022) 88, https://doi.org/10.1016/J.PECS.2021.100956.

[16] A. D'Anna, Combustion-formed nanoparticles, Proc. Combust. Inst. 32 (2009) 593–613, https://doi.org/10.1016/j.proci.2008.09.005.

[17] H. Wang, Formation of nascent soot and other condensed-phase materials in flames, Proc. Combust. Inst. 33 (2011) 41–67, https://doi.org/10.1016/j.proci.2010.09.009.

[18] M. Zhong, X. Wang, Y. Huang, L. Li, S. Gao, Y. Tian, et al., Anthracite-derived carbon-based electrode materials for high performance lithium ion capacitors, Fuel Process. Technol. 228 (2022), 107146, https://doi.org/10.1016/j.fuproc.2021.107146.

[19] P. Zhao, B. Shen, J. Wang, F. Lu, P. Yuan, The production and electrochemical performance of carbon nano-materials derived from plastics over nickel-based catalysts with different supports, Fuel Process. Technol. 249 (2023), 107853, https://doi.org/10.1016/j.fuproc.2023.107853.

[20] D. Guo, D. Feng, Y. Zhang, Y. Zhang, Y. Zhao, Z. Zhou, et al., Carbon material-TiO2 for photocatalytic reduction of CO2 and degradation of VOCs: a critical review, Fuel Process. Technol. 231 (2022), 107261, https://doi.org/10.1016/j.fuproc.2022.107261.

[21] M.R. Mulay, A. Chauhan, S. Patel, V. Balakrishnan, A. Halder, R. Vaish, Candle soot: Journey from a pollutant to a functional material, Carbon N Y 144 (2019) 684–712, https://doi.org/10.1016/j.carbon.2018.12.083.

[22] K.D. Esmeryan, C.E. Castano, A.H. Bressler, M. Abolghasemibizaki, R. Mohammadi, Rapid synthesis of inherently robust and stable superhydrophobic carbon soot coatings, Appl. Surf. Sci. 369 (2016) 341–347, https://doi.org/10.1016/j.apsusc.2016.02.089.

[23] B. Zhang, D. Wang, B. Yu, F. Zhou, W. Liu, Candle soot as a supercapacitor electrode material, RSC Adv. 4 (2014) 2586–2589, https://doi.org/10.1039/C3RA42507J.

[24] A. Baldelli, K.D. Esmeryan, O. Popovicheva, Turning a negative into a positive: trends, guidelines and challenges of developing multifunctional non-wettable coatings based on industrial soot wastes, Fuel 301 (2021), 121068, https://doi.org/10.1016/j.fuel.2021.121068.

[25] M. Commodo, G. De Falco, A. Bruno, C. Borriello, P. Minutolo, A. D'Anna, Physicochemical evolution of nascent soot particles in a laminar premixed flame: from nucleation to early growth, Combust. Flame (2015) 162, https://doi.org/10.1016/j.combustflame.2015.07.022.

[26] G.A. Kelesidis, E. Goudeli, S.E. Pratsinis, Flame synthesis of functional nanostructured materials and devices: surface growth and aggregation, Proc. Combust. Inst. 36 (2017) 29–50, https://doi.org/10.1016/j.proci.2016.08.078.

[27] G. De Falco, R. Ciardiello, M. Commodo, P. Del Gaudio, P. Minutolo, A. Porta, et al., TIO2 nanoparticle coatings with advanced antibacterial and hydrophilic properties prepared by flame aerosol synthesis and thermophoretic deposition, Surf. Coat. Technol. (2018) 349, https://doi.org/10.1016/j.surfcoat.2018.06.083.

[28] G. De Falco, M. Commodo, C. Bonavolontà, G.P. Pepe, P. Minutolo, A. D'Anna, Optical and electrical characterization of carbon nanoparticles produced in laminar premixed flames, Combust. Flame (2014) 161, https://doi.org/10.1016/j.combustflame.2014.05.021.

[29] G. De Falco, M. Commodo, M. Barra, F. Chiarella, A. D'Anna, A. Aloisio, et al., Electrical characterization of flame-soot nanoparticle thin films, Synth. Met. (2017) 229, https://doi.org/10.1016/j.synthmet.2017.05.008.

[30] P. Minutolo, G. De Falco, M. Commodo, A. Aloisio, A. D'Anna, Temperature sensing with thin films of flame-formed carbon nanoparticles, Appl. Sci. 12 (2022) 7714, https://doi.org/10.3390/app12157714.

[31] H.F. Calcote, R.N. Pease, Electrical properties of flames. Burner flames in longitudinal electric fields, Ind. Eng. Chem. 43 (1951) 2726–2731, https://doi.org/10.1021/ie50504a032.

[32] J. Lawton, F.J. Weinberg, Electrical Aspects of Combustion, Clarendon Press, Oxford, U.K., 1969.

[33] A. Fialkov, Investigations on ions in flames, Prog. Energy Combust. Sci. 23 (1997) 399–528, https://doi.org/10.1016/S0360-1285(97)00016-6.

[34] M. Cha, S. Lee, K. Kim, S. Chung, Soot suppression by nonthermal plasma in coflow jet diffusion flames using a dielectric barrier discharge, Combust. Flame 141 (2005) 438–447, https://doi.org/10.1016/j.combustflame.2005.02.002.

[35] A. Parisi, G. De Falco, M. Sirignano, P. Minutolo, M. Commodo, C. Carotenuto, et al., Modelling the electrophoretically-enhanced in-flame deposition of carbon nanoparticles, J. Aerosol Sci. (2023) 172, https://doi.org/10.1016/j.jaerosci.2023.106193.

[36] A.V. Raghu, K.K. Karuppanan, B. Pullithadathil, Highly sensitive, temperature-independent oxygen gas sensor based on anatase TiO $_2$ nanoparticle grafted, 2D mixed valent VO $_x$ nanoflakelets, ACS Sens. 3 (2018) 1811–1821, https://doi.org/10.1021/acssensors.8b00544.

[37] B.C. Marin, S.E. Root, A.D. Urbina, E. Aklile, R. Miller, A.V. Zaretski, et al., Graphene–metal composite sensors with near-zero temperature coefficient of resistance, ACS Omega 2 (2017) 626–630, https://doi.org/10.1021/acsomega.7b00044.
[38] S. Gong, D. Wu, Y. Li, M. Jin, T. Xiao, Y. Wang, et al., Temperature-independent piezoresistive sensors based on carbon nanotube/polymer nanocomposite, Carbon N Y 137 (2018) 188–195, https://doi.org/10.1016/j.carbon.2018.05.029.
[39] M. Commodo, K. Kaiser, G. De Falco, P. Minutolo, F. Schulz, A. D'Anna, et al., On the early stages of soot formation: molecular structure elucidation by high-resolution atomic force microscopy, Combust. Flame (2019) 205, https://doi.org/10.1016/j.combustflame.2019.03.042.
[40] M. Commodo, A. D'Anna, G. De Falco, R. Larciprete, P. Minutolo, Illuminating the earliest stages of the soot formation by photoemission and Raman spectroscopy, Combust. Flame (2017) 181, https://doi.org/10.1016/j.combustflame.2017.03.020.
[41] S. Veronesi, M. Commodo, L. Basta, G. De Falco, P. Minutolo, N. Kateris, et al., Morphology and electronic properties of incipient soot by scanning tunneling microscopy and spectroscopy, Combust. Flame 243 (2022), 111980, https://doi.org/10.1016/j.combustflame.2021.111980.
[42] M.M. Maricq, A comparison of soot size and charge distributions from ethane, ethylene, acetylene, and benzene/ethylene premixed flames, Combust. Flame 144 (2006) 730–743, https://doi.org/10.1016/j.combustflame.2005.09.007.
[43] G. De Falco, M. Commodo, C. Bonavolontà, G.P. Pepe, P. Minutolo, A. D'Anna, Optical and electrical characterization of carbon nanoparticles produced in laminar premixed flames, Combust. Flame (2014) 161, https://doi.org/10.1016/j.combustflame.2014.05.021.
[44] M. Ahmadipour, W.K. Cheah, M.F. Ain, K.V. Rao, Z.A. Ahmad, Effects of deposition temperatures and substrates on microstructure and optical properties of sputtered CCTO thin film, Mater. Lett. 210 (2018) 4–7, https://doi.org/10.1016/j.matlet.2017.08.121.
[45] G. De Falco, G. Mattiello, M. Commodo, P. Minutolo, X. Shi, A. D'Anna, et al., Electronic band gap of flame-formed carbon nanoparticles by scanning tunneling spectroscopy, Proc. Combust. Inst. (2021) 38, https://doi.org/10.1016/j.proci.2020.07.109.
[46] G.A. Kelesidis, C.A. Bruun, S.E. Pratsinis, The impact of organic carbon on soot light absorption, Carbon N Y 172 (2021) 742–749, https://doi.org/10.1016/j.carbon.2020.10.032.
[47] M. Commodo, G. De Falco, A. Bruno, C. Borriello, P. Minutolo, A. D'Anna, Physicochemical evolution of nascent soot particles in a laminar premixed flame: from nucleation to early growth, Combust. Flame (2015) 162, https://doi.org/10.1016/j.combustflame.2015.07.022.
[48] P. Minutolo, M. Commodo, A. D'Anna, Optical properties of incipient soot, Proc. Combust. Inst. 39 (2023) 1129–1138, https://doi.org/10.1016/j.proci.2022.09.019.
[49] P. Bruschi, P. Cagnoni, A. Nannini, Temperature-dependent Monte Carlo simulations of thin metal film growth and percolation, Phys. Rev. B 55 (1997) 7955–7963, https://doi.org/10.1103/PhysRevB.55.7955.
[50] P. Bruschi, A. Nannini, Current vs. voltage characteristics of ion-beam-grown polymer-metal granular thin films, Thin Solid Films 201 (1991) 29–38, https://doi.org/10.1016/0040-6090(91)90151-M.